

Perovskites

Efficient (> 20 %) and Stable All-Inorganic Cesium Lead Triiodide Solar Cell Enabled by Thiocyanate Molten Salts

Bingcheng Yu[†], Jiangjian Shi[†], Shan Tan, Yuqi Cui, Wenyan Zhao, Huijue Wu, Yanhong Luo, Dongmei Li,^{*} and Qingbo Meng^{*}

Abstract: Besides widely used surface passivation, engineering the film crystallization is an important and more fundamental route to improve the performance of all-inorganic perovskite solar cells. Herein, we have developed a urea-ammonium thiocyanate (UAT) molten salt modification strategy to fully release and exploit coordination activities of SCN^- to deposit high-quality CsPbI_3 film for efficient and stable all-inorganic solar cells. The UAT is derived by the hydrogen bond interactions between urea and NH_4^+ from NH_4SCN . With the UAT, the crystal quality of the CsPbI_3 film has been significantly improved and a long single-exponential charge recombination lifetime of over 30 ns has been achieved. With these benefits, the cell efficiency has been promoted to over 20 % (steady-state efficiency of 19.2 %) with excellent operational stability over 1000 h. These results demonstrate a promising development route of the CsPbI_3 related photoelectric devices.

Introduction

Integrating with narrow-band gap (E_g) silicon or chalcopyrite to afford a tandem solar cell is one of the most lucrative application outputs of lead halide perovskite materials.^[1–3] In those reported perovskite tandem solar cells, hybrid perovskites composed of mixed cations (including formamidinium

(FA^+), methylammonium (MA^+) or Cs^+) and I^-/Br^- mixed anions are used for top wide-band gap absorber with E_g ranging from 1.65 to 1.75 eV. Although excellent power conversion efficiency (PCE) has been achieved, the high volatility and rotation freedom of MA^+ and severe light-induced phase segregation of I/Br alloying are still giant threat to the operational stability of these cells.^[4–9] Dimensional engineering with long-chain cations could provide stable wide- E_g perovskite by avoiding I/Br alloying; however, there is still a large gap in the PCE between the quasi-2D and the conventional mixed-ion perovskites, which will be a challenge to manipulate the lattice orientation of quasi-2D perovskites on a textured bottom cell.^[10–15]

Alternatively, black-phase all-inorganic cesium lead triiodide (CsPbI_3) is an ideal perovskite candidate with E_g of about 1.67 eV, which does not have any volatile component and exhibits highly thermal and photoelectrical stabilities.^[16–20] The CsPbI_3 solar cell has already been a hot research topic in recent years owing to these advantages and impressive progresses. The performance enhancement of the CsPbI_3 solar cell mainly benefits from two aspects, one is the utilization of dimethylammonium iodide (DMAI) or DMAPbI₃ to tune intermediate phase and crystallization processes of the CsPbI_3 , which helps to achieve pure and stable CsPbI_3 black phase with relatively low annealing temperature.^[21–26] The other one is the surface passivation toward the CsPbI_3 layer by introducing long-chain organic ammonium halides, such as octylammonium iodide, phenyltrimethylammonium chloride and choline iodide.^[16,23,27,28] With these efforts, the PCE of this solar cell has been improved to around 20%.^[27] Nonetheless, compared to the hybrid perovskite, these efficient CsPbI_3 solar cells still suffer from large photovoltage deficit due to severe non-radiative charge recombination.^[29,30] Currently, even introducing surface passivation, the charge lifetime of a pure 3D CsPbI_3 in these cells is only in a range of 10–20 ns.^[23,27] This means that defects in the bulk CsPbI_3 film play a more fundamental role in causing charge recombination loss of the cell.^[30–34] Therefore, it is of high significance to focus more efforts on exploring effective approaches to eliminating bulk defect of the CsPbI_3 .

Coordination engineering to tune crystallization process by forming lead or iodide complexes is an effective strategy to improve crystal quality and suppress defects of the perovskite, which has been successfully applied in hybrid perovskite solar cells.^[35–44] Among those coordination additives, thiocyanate (SCN^-) (e.g. $\text{Pb}(\text{SCN})_2$, MASCN, FASCN or GuaSCN (Gua: guanidinium)) has been demonstrated to have a very positive effect on regulating the Pb-I octahedron structure and film



[*] B. Yu,^[†] J. Shi,^[†] S. Tan, Y. Cui, W. Zhao, H. Wu, Prof. Y. Luo, Prof. D. Li, Prof. Q. Meng
 Key Laboratory for Renewable Energy
 Chinese Academy of Sciences (CAS)
 Beijing Key Laboratory for New Energy Materials and Devices
 Beijing National Laboratory for Condensed Matter Physics
 Institute of Physics, Beijing 100190 (China)
 E-mail: dmli@iphy.ac.cn
 qbmeng@iphy.ac.cn

Prof. Q. Meng
 Center of Materials Science and Optoelectronics Engineering,
 University of Chinese Academy of Sciences
 Beijing 100049 (China)

B. Yu,^[†] S. Tan, Y. Cui, Prof. Y. Luo, Prof. D. Li
 School of Physical Sciences
 University of Chinese Academy of Sciences
 Beijing 100049 (China)

Prof. Y. Luo, Prof. D. Li, Prof. Q. Meng
 Songshan Lake Materials Laboratory
 Dongguan, Guangdong 523808 (China)

[†] These authors contributed equally to this work.

 Supporting information and the ORCID identification number(s) for the author(s) of this article can be found under:
 <https://doi.org/10.1002/anie.202102466>.

morphology.^[40,42–45] Recently, Lu et al. reported low-defect photoactive α -phase FAPbI_3 obtained at relatively low temperature by the assistance of MASCN vapor treatment. This vapor process has considerably weakened the Coulombic interaction between MA^+ and SCN^- and thus has fully released the coordination activity of SCN^- .^[44]

In this respect, we develop a more easily operated solution modification approach for high-quality CsPbI_3 film, in which the coordination-active SCN^- is realized through a formation of urea-ammonium thiocyanate (UAT) molten salt. The UAT is derived from heating the mixture of NH_4SCN and urea. The formation of NH_4^+ -urea supramolecular cations by hydrogen bonds can weaken the Coulombic bonding between cations and SCN^- anions and thus make the SCN^- have stronger coordination ability with the Pb-I octahedron. The UAT modification has improved the CsPbI_3 film morphology, significantly suppressing film defects and the non-radiative charge recombination. Based on the optimal UAT, we finally achieved a highly efficient CsPbI_3 solar cell with the PCE of over 20.0% and high fill factor of 0.843. Besides, the cell exhibits high operational stability with almost no PCE degradation after 1000 h working under continuous light illumination and bias voltage (close to maximum power point). Therefore, this work demonstrates a promising development route of the CsPbI_3 related photoelectric devices.

Results and Discussion

In this work, our UAT molten salt is obtained by mixing a certain ratio of NH_4SCN and urea powders together and then heating at 100°C under continuous stirring. This mixture system can be easily melted shortly after heating to afford a transparent and colorless liquid finally, as shown in the Supporting Information, Figure S1. When it is incorporated as

an additive to fabricate the CsPbI_3 film, an observable influence on the crystal structure of DMAPbI_3 can be seen, as indicated by X-ray diffraction (XRD) results in Figure 1a. When the DMAPbI_3 powder is ground with UAT to afford DMAPbI_3 -UAT complexes, a series of new and unknown XRD peaks appear at around 5.6° , 7.8° , 14.7° , 23.7° , 24.6° etc. Furthermore, the main XRD peak of the UAT is slightly shifted to the low angle direction. These changes in XRD patterns are good indication for strong interactions between these two materials. When the UAT is only used as an additive in the DMAPbI_3 solution, the lattice structure of DMAPbI_3 phase (i.e. XRD peak position) is little influenced, which ensures the function of DMAPbI_3 in forming CsPbI_3 perovskite. However, with the UAT modification, the main peak of DMAPbI_3 phase exhibits a 10-fold intensity enhancement with the peak width being obviously decreased. This result indicates a higher lattice ordering degree and crystal quality of the DMAPbI_3 film. In addition to the DMAPbI_3 phase, two new peaks at 5.7° and 7.2° can also be clearly seen. These two peaks are similar to that appear in the DMAPbI_3 -UAT sample and may arise from a new layered phase due to the incorporation of large-size NH_4^+ -urea cations.

XRD intensity of the final CsPbI_3 film is also enhanced with these influences of the UAT, and the film morphology exhibits a clear improvement. As in Figure 1b, some large pinholes can be seen in the control CsPbI_3 film, whereas these pinholes in the UAT modified film have been effectively eliminated. The UAT modified film exhibits a much more uniform SEM image with larger grain sizes (Figure 1c) and smaller surface roughness ($R_a = 18.7$ nm) (Figure 1d). We also measured surface potential and energy band position of these two CsPbI_3 films with KPFM and UPS (Figure 1e,f). The modified CsPbI_3 film exhibits a higher work function by about 80 meV whereas an identical valence band position of 1.47 eV (vs. Fermi energy) for these two films (Figure S2).

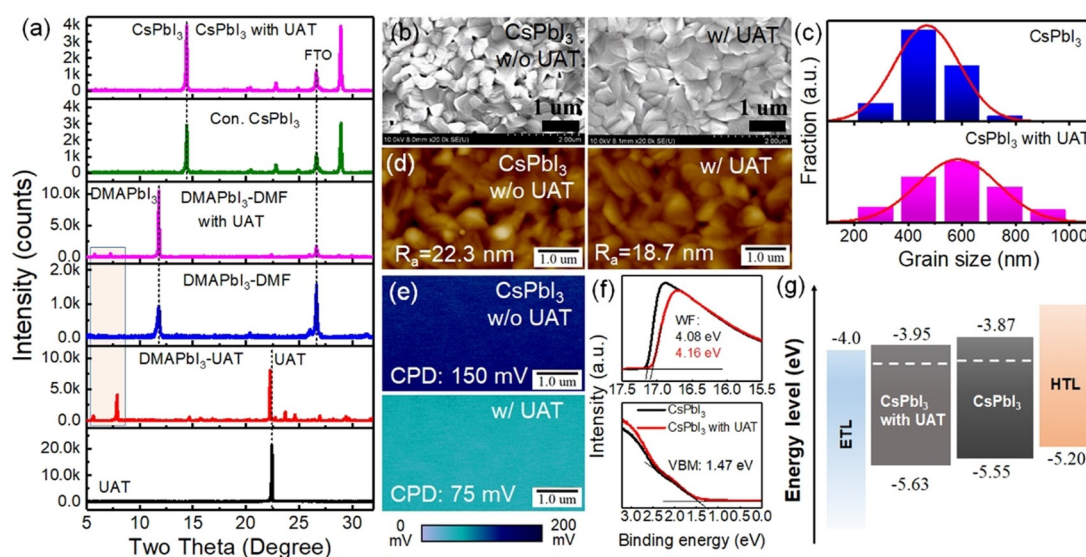


Figure 1. Characterizations of CsPbI_3 films. a) XRD patterns of DMAPbI_3 and CsPbI_3 modified by the UAT. Dashed lines depict characteristic XRD peaks of DMAPbI_3 , CsPbI_3 , FTO and UAT. b) Scanning electron microscope (SEM) image, c) grain size distribution, d) atomic force microscope morphology, e) Kelvin probe force microscopy (KPFM) surface potential distribution and f) ultraviolet photoelectron spectroscopy (UPS) of CsPbI_3 films prepared with (w/) or without (w/o) the UAT additive. g) Energy band alignment of the cell.

Based on this information, the band alignment of the cell is given in Figure 1g, indicating that the energy band of the modified film is shifted to a deeper position. This shift increases the energy difference between the conduction band minimum (CBM) of TiO_2 and the valence band maximum (VBM) of CsPbI_3 as well as the difference between the CBM of CsPbI_3 and the lowest unoccupied molecular orbital of the Spiro-OMeTAD (Spiro-OMeTAD: 2,2',7,7'-tetrakis [N, N-di(4-methoxyphenyl) amino]-9,9,0-spirofluorene), which can help reduce interfacial charge recombination loss.

Furthermore, the influence of UAT introduction on the cell performance has been investigated (see the detailed fabrication process in the Supporting Information, Figures S3,S4). The device configuration of FTO glass/ TiO_2 / CsPbI_3 /Spiro-OMeTAD/Au, is adopted, as shown in Figure 2a. For comparison, NH_4SCN and urea are also separately used as the additive, and a precursor solution containing both NH_4SCN and urea is also used (defined as $\text{NH}_4\text{SCN} + \text{urea}$), which are added one by one. The current-voltage (I - V) curves of champion cells derived from different precursors are shown in Figure 2b. When no additive is added, the solar cell (Con.) exhibits a PCE of 17.86% with short-circuit current density (J_{SC}) of 20.7 mA cm^{-2} , open-circuit voltage (V_{OC}) of 1064 mV and fill factor (FF) of 0.81 (Supporting Information, Table S1). This cell performance is comparable to that of most control cells reported previously. When only NH_4SCN or urea are added, the PCE slightly increases to 18.33% and 18.12%, respectively. Although the cell V_{OC} increases by about 25 mV, the addition of $\text{NH}_4\text{SCN} + \text{urea}$ has little influence on the PCE because of the reduced

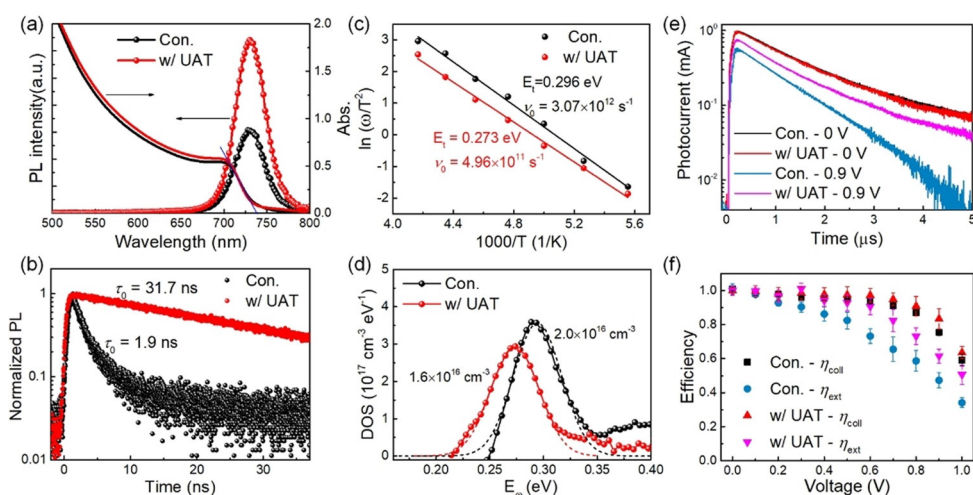


Figure 3. Defect and charge recombination of CsPbI_3 films. a) UV/Vis absorption and steady-state photoluminescence (PL) spectra and b) transient PL of CsPbI_3 films with or without the UAT modification. c), d) Defect measurement of CsPbI_3 films in solar cells by thermal admittance spectroscopy (TAS), including (c) Arrhenius relationship between $\ln(\omega/T^2)$ and $1/T$ (ω is the frequency of the maxima of $\omega \times dC/d_{\text{eff}}$, C is the capacitance and T is the thermodynamics temperature) to evaluate the defect energy level and (d) density of states (DOS) distribution of the measured defect. e) Transient photocurrent of the cells under a 0 or 0.9 V bias voltage. f) Charge collection (η_{coll}) and extraction (η_{ext}) efficiencies derived from the bias voltage dependent transient photocurrents.

FF (0.797). Comparatively, the UAT incorporation leads to a high PCE of approaching 19% with enhancement in J_{SC} , V_{OC} and FF. This is comparable to that of the recently reported cells using $\text{Zn}(\text{C}_6\text{F}_5)_2$ or PTACl as surface modifications.^[23,46] As shown in Figure 2c, V_{OC} of the UAT based cell has improved by more than 40 mV compared to the control one, implying that the crystal quality of the CsPbI_3 film has indeed been promoted. This enhancement is supposed to be related to the Pb-SCN coordination interaction.

Non-radiative charge recombination in the CsPbI_3 has also been significantly suppressed, as shown by steady-state and transient PL spectra (Figure 3a,b). Under light excitation, the CsPbI_3 film emits photons through band edge direct recombination. With the UAT modification, the PL intensity exhibits a two-fold enhancement. Impressively, the modified CsPbI_3 film has a long and single-exponential PL lifetime of 31.7 ns, which is 16 times higher than that of the control sample (Supporting Information, Table S2). Defect proper-

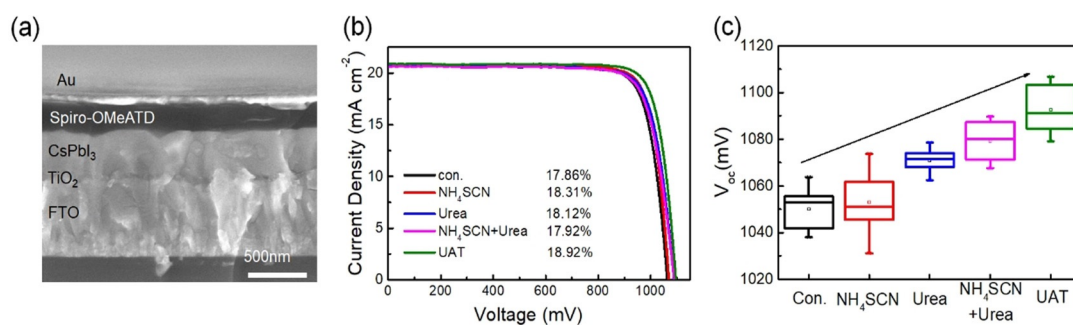


Figure 2. a) Cross-sectional SEM image of the complete cell. b) Current-voltage curves of the CsPbI_3 solar cell with different modifications. The PCE of each cell is given inside the Figure. c) Statistics of the V_{OC} of the cells.

ties of our prepared CsPbI₃ film are further quantitatively evaluated by using TAS method. Capacitance–frequency (*C-f*) characteristics of a complete cell at temperatures (*T*) ranging from 180 to 300 K were measured (Supporting Information, Figure S5). It can be seen from the *C-f* spectra that, the capacitance increases in the intermediate-high frequency region, which is arisen from defect response. Based on the Arrhenius relationship between $\ln(\omega/T^2)$ and $1/T$ (ω is the angular frequency of the maxima of $\omega \times d_c/d_\omega$), defect energy level (E_t) and attempt-to-escape frequency (ν_0) are derived and shown in Figure 3c, where ν_0 is a characteristic parameter to reflect the charge capturing activity of a defect. With the UAT modification, E_t of the CsPbI₃ film has been slightly shifted from 0.296 to 0.273 eV and ν_0 has been reduced by about an order of magnitude from 3.07×10^{12} to $4.96 \times 10^{11} \text{ s}^{-1}$. This large reduction in the ν_0 perhaps arises from a higher lattice ordering degree of the modified sample, which helps to suppress local atom displacements occurred in the electron non-radiative transition processes. The density of states (DOS) of these two samples is further derived as $\text{DOS}(E_\omega) = -V_D/(eW)\omega/(KT)d_c/d_\omega$, where V_D is the depletion potential of the measured device, e is the electron charge, W is the depletion width and K is the Boltzmann constant. As seen in Figure 3d, both samples have a Gaussian-type defect distribution and similar energy broadening of about 22.5 meV. The UAT modification slightly decreases the defect density of CsPbI₃ film from 2.0 to $1.6 \times 10^{16} \text{ cm}^{-3}$. These reduction in both the defect density and the charge capturing activity finally leads to much longer charge-carrier lifetime of the CsPbI₃ film, which could help decrease charge loss in the bulk perovskite.

Charge loss of the cell when it works is further quantitatively measured by using a modulated electrical transient method (Detailed equations and procedures for the calculation are given in the Supporting Information).^[47] Transient photocurrent results of the cells under 0 or 0.9 V bias voltage are shown in Figure 3e. At 0 V, these two cells exhibit similar photocurrent decay behaviors (peak value and decay time), indicating their similar charge extraction and transport properties under the short-circuit condition. At a high bias voltage of 0.9 V, non-radiative charge recombination increases to result in obvious difference in photocurrent between these two cells. Compared to the UAT modified sample, the photocurrent of the control cell exhibits a much lower peak value and a faster decay. The lower peak value indicates a lower extraction efficiency (η_{ext}) for the charge transporting from bulk perovskite into the transporting layers while the faster decay means lower charge collection efficiency (η_{coll}). Integrated charge and decay time of the photocurrent, η_{ext} and η_{coll} of these two cells at different voltages are shown in

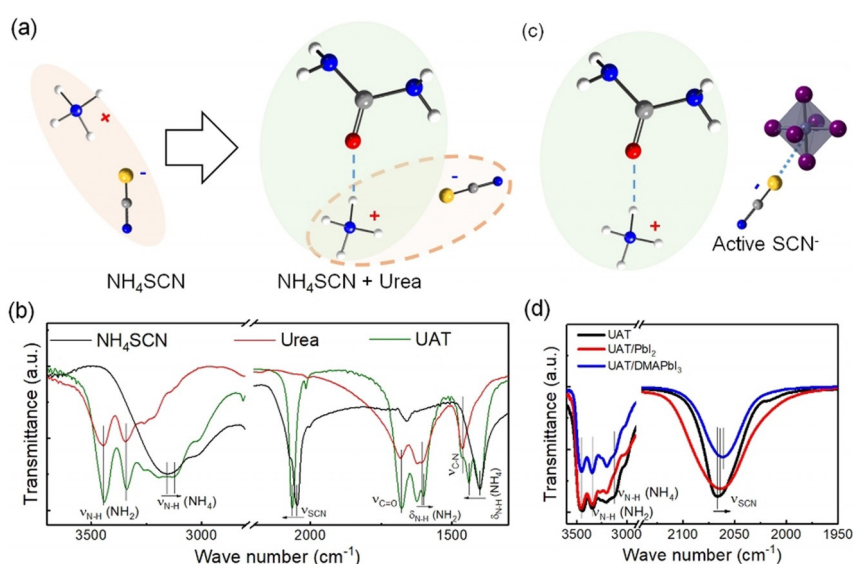


Figure 4. a) Diagram of the molecule structure transition from NH₄SCN to UAT. Dashed straight lines depict the hydrogen bonds between NH₄⁺ and urea and the dashed ellipse means a weakened Coulombic bond between NH₄⁺ and SCN⁻. b) Fourier transform infrared spectra (FTIR) of NH₄SCN, urea and the UAT. Vibration bands of varied chemical groups are marked out by short straight lines and their shift is depicted by short arrows. c) Diagram of interaction between the UAT and the Pb-Octahedron of perovskite precursors. d) FTIR results of UAT when they are mixed with PbI₂ and DMAPbI₃.

Figure 3f. It can be seen that, the η_{ext} of the UAT modified cell has been obviously improved, agreeing well with the PL and defect measurement results and finally leading to a higher V_{OC} and FF of the cell.

The formation of molten salt can be attributed to relatively weak inter-ionic interaction and intermolecular interaction with urea, in comparison with pure NH₄SCN, as schematically shown in Figure 4a. The hydrogen bond between NH₄⁺ and urea leads to the formation of larger cations. These interactions are studied by FTIR spectra. For the NH₄SCN, its characteristic IR absorption peaks including N-H stretching vibration [$\nu_{\text{N-H}}(\text{NH}_4)$] at 3155 cm⁻¹, N-H bending vibration [$\delta_{\text{N-H}}(\text{NH}_4)$] at 1401 cm⁻¹ and SCN stretching vibration (ν_{SCN}) at 2047 cm⁻¹ can be clearly seen in the spectrum. For the urea, characteristic IR absorption peaks including two N-H stretching vibrations [$\nu_{\text{N-H}}(\text{NH}_2)$] at 3344 and 3445 cm⁻¹, respectively, N-H bending vibration [$\delta_{\text{N-H}}(\text{NH}_2)$] at 1605 cm⁻¹, C=O stretching vibration ($\nu_{\text{C=O}}$) at 1682 cm⁻¹ and C-N stretching vibration ($\nu_{\text{C-N}}$) at 1463 cm⁻¹ can be distinguished. After forming the UAT, IR peak shifts can be clearly seen in the spectra, as depicted by arrows in Figure 4b. Specifically, $\nu_{\text{N-H}}(\text{NH}_4)$ peak is shifted to lower wavenumbers by 35 cm⁻¹; $\delta_{\text{N-H}}(\text{NH}_4)$ peak is splitted into two peaks and the new one is shifted to a higher wavenumber by 40 cm⁻¹ compared to the original one. IR peaks corresponding to the urea are also slightly shifted and especially $\delta_{\text{N-H}}(\text{NH}_2)$ is shifted to a lower wavenumber position. These IR peak shifts suggest the formation of hydrogen bonds between NH₄⁺ and urea molecules. This newly formed NH₄⁺-urea cation can obviously weaken their interaction to the SCN⁻, thus enhances the freedom of the SCN⁻, as confirmed by the blueshift of ν_{SCN} peak.

In terms of the above results, the interaction between the active SCN^- in the UAT and the Pb-I octahedron in perovskite precursors is suggested in Figure 4c. This interaction is confirmed by a low-wavenumber shift (from 2066 to 2061 cm^{-1}) of ν_{SCN} peak when the UAT is mixed with DMAPbI_3 , as shown in Figure 4d. The unchanged $\nu_{\text{N-H}}$ (NH_4^+) peak also indicates that the NH_4^+ -urea structure has not been influenced. Comparatively, SCN^- of NH_4SCN and C=O of urea exhibit lower coordination activities with the Pb-I octahedron, and no ν_{SCN} or $\nu_{\text{C=O}}$ peak shift can be observed when each of them is mixed with PbI_2 or DMAPbI_3 , as shown in Figure S6. NH_4^+ of NH_4SCN may have an interaction with the DMAPbI_3 due to a slight shift of $\nu_{\text{N-H}}$ (NH_4^+) peak. As such, we preliminarily conclude that the introduction of UAT has realized our initial purpose to release free coordination-active SCN^- groups.

The cell performance has been further improved by optimizing the concentration and the urea/ NH_4SCN ratio of the UAT (Supporting Information, Tables S3–S6). Statistical PCE of the cells with different modification conditions is shown in Figure 5a. With 6 mM UAT, the cell exhibits the highest PCE and this trend is independent to the component ratio. At higher UAT concentration, the aggregation of perovskite crystals and large voids appear, resulting in poor cell PCE (more details can be seen in the Supporting Information, Figures S7–S9). Under this optimal UAT concentration, the urea/ NH_4SCN ratio of 1.4 (denoted as UAT-1.4 for clarity) can lead to a higher cell PCE, which is about 9% (averaged value) superior over the control cells. Compo-

nent ratio is an important variable that can influence physical and chemical properties of the molten salt, such as ion or molecule structure, melting and boiling points. Here, ion conductivity (σ) measurement was used to reflect the structural freedom of the SCN^- in the UAT because the ion transport is mainly contributed from the SCN^- owing to its smaller size and linear structure. As in Figure 5b, the UAT-1.4 sample has the largest σ , implying that its SCN^- has the highest freedom to interact with the Pb-I octahedrons. Further, it can be found that the cell PCE is positively related to the σ , especially when the component ratio is not larger than 1.5. This means that the PCE improvement is mainly attributed to the enhancement in the coordination activity of the SCN^- . Interestingly, different from the PCE, the UAT-1.0 and UAT-1.3 based cells exhibit unsatisfied FF. This phenomenon is similar to that observed in the NH_4SCN + Urea based solar cells, implying that UAT at low component ratio may have not functioned as designed.

From the perspective of UAT formation mechanism, it is supposed that further increasing the urea/ NH_4SCN ratios may be able to promote the NH_4^+ -urea bonding and thus increasing the cation size and weakening the Coulombic bondage of the SCN^- . However, both the σ and the PCE results at high urea/ NH_4SCN ratios (≥ 1.5) seem not to support this scenario. Obviously, besides the SCN^- , the cations (such as NH_4^+ or urea- NH_4^+) could also influence the crystallization process of the perovskite film. The change of the cation in the UAT and its influence has also been studied by FTIR, thermogravimetric (TG), DSC, XRD and SEM analysis. The splitting of

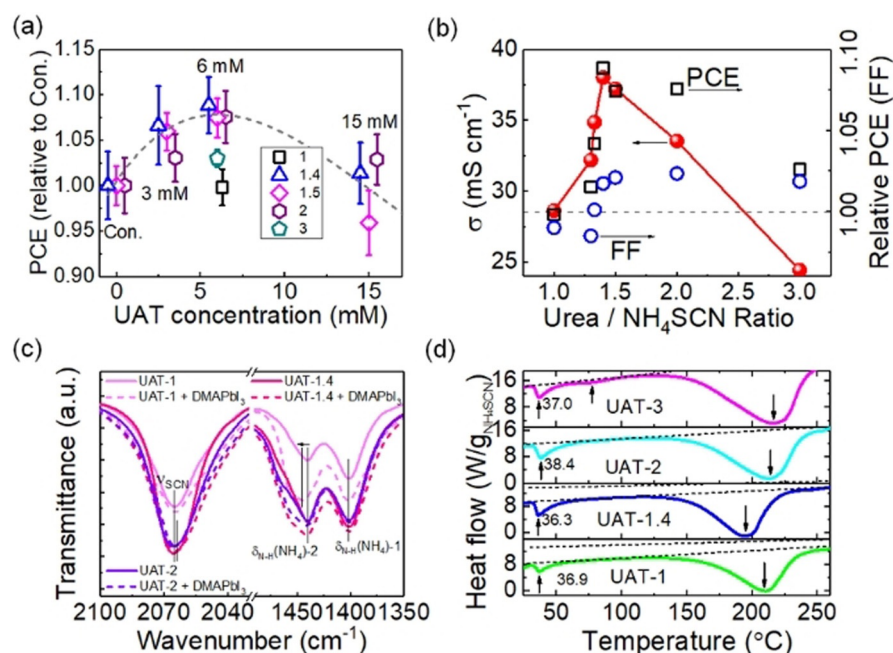


Figure 5. UAT optimizations for higher cell performance. a) Statistical PCE of the cells. Different concentrations of the UAT composed of different NH_4SCN /urea ratios are used. The dashed line is a guidance for eyes. b) Ion conductivity of the UAT, cell PCE and FF as a function of the urea/ NH_4SCN ratio. c) FTIR spectra [ν_{SCN} and $\delta_{\text{N-H}}(\text{NH}_4)$] of the UAT before and after mixed with the DMAPbI_3 . d) Differential scanning calorimetry (DSC) analysis of the UAT. To compare intensity of endothermic signals between different UAT samples, the mass of the NH_4SCN in the UAT is used for the heat flow calibration.

The splitting of $\delta_{\text{N-H}}(\text{NH}_4)$ IR peak and the relative intensity between the two split peaks (depicted as $\delta_{\text{N-H}}(\text{NH}_4)$ -1 and $\delta_{\text{N-H}}(\text{NH}_4)$ -2) can be used to reflect the coordination bond quantity of NH_4^+ . As in Figure 5c, when increasing the urea/ NH_4SCN ratio (from 1.0 to 2.0 shown here), the relative intensity of the $\delta_{\text{N-H}}(\text{NH}_4)$ -2 peak is obviously enhanced. And when mixed with DMAPbI_3 , the interaction between urea and NH_4^+ in UAT-1.4 and UAT-2 can be sustained as indicated by their unchanged $\delta_{\text{N-H}}(\text{NH}_4)$ -2 peak position. Comparatively, for UAT-1, when interacting with DMAPbI_3 , the $\delta_{\text{N-H}}(\text{NH}_4)$ -2 peak is shifted to a higher wavenumber whereas the ν_{SCN} is not shifted, implying that the NH_4^+ instead of the SCN^- in the UAT is coordinated with the Pb-I octahedrons. This interaction form seems to have little influence on the cell PCE (same as NH_4SCN + Urea; Supporting Information, Figure S10). The difference in the coordination bond quantity is also confirmed by TG and DSC results (Figure 5d; Supporting Information, Figure S11). At 36–38 $^{\circ}\text{C}$, all the UATs exhibit an endo-

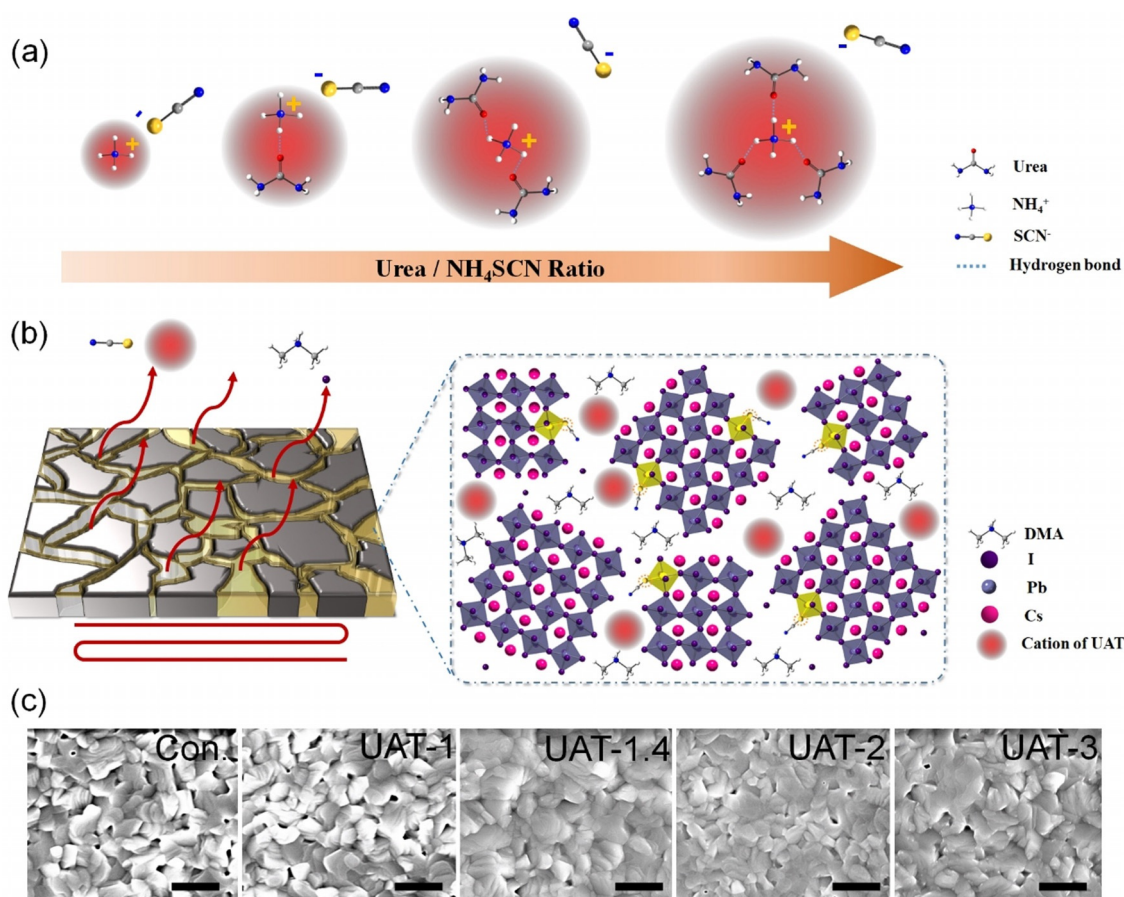


Figure 6. a) Possible NH_4^+ -urea cation structure of the UAT with different component ratio. b) Perovskite crystal growth and additive volatilization of the film. Large NH_4^+ -urea cations mainly distribute in the grain boundaries of the perovskite and thus have a non-negligible influence on the crystal fusion process. c) Top-view SEM images of the CsPbI_3 films modified with different UATs. Scale bar: 1 μm .

thermic peak that may arise from the hydrogen bond between NH_4^+ and urea. Compared to other UATs, the UAT-1 has the weakest endothermic intensity, indicating the lowest coordination bond quantity. At higher urea/ NH_4SCN ratios, for example the UAT-3, a new broad endothermic peak appears at 76 °C, implying that excess urea in the UAT could bring some new interaction and make the NH_4^+ -urea coordination structure more complicated.

For clarity, possible NH_4^+ -urea cation structure and their influence on the crystallization process of the perovskite film are schematically shown in Figure 6. As in Figure 6a, at a higher component ratio, NH_4^+ could coordinate with more urea molecules, resulting in a larger cation, which main XRD peak of the newly formed layered-type phase is shifted from 7.2° to 5.7° (Supporting Information, Figure S12). Furthermore, these large cations may connect with each other by possible H–N⋯H interactions, forming more complicated structures, such as supermolecular frameworks. In perovskite nucleation and crystal growth processes, these large NH_4^+ -urea structures may mainly distribute around the precursor perovskite clusters or in the crystal nucleus boundaries, which will affect perovskite crystallization and growth, as shown in Figure 6b. In this case, the volatilization properties of the UAT is an important variable in influencing the crystal quality of the final perovskite film. Recent work exhibited that

accelerating the removing of organic components in the film will afford better perovskite films.^[27,48] Volatilization behavior of these UATs can be directly observed by DSC and TG. Among all the UATs, the UAT-1.4 has the lowest volatilization onset temperature as well as the largest gravity loss in the annealing process, and its NH_4^+ -urea cation may have the least unfavorable influence on the perovskite crystallization. As such, the CsPbI_3 film with the UAT-1.4 modification exhibits the best surface morphology, as in Figure 6c and the Supporting Information, Figure S13. X-ray photoelectron spectroscopy characterization further confirms that, no obvious N and S element signals are detectable in the CsPbI_3 film treated with UAT, that is, there is basically no residual chemical in final CsPbI_3 films after high temperature annealing (Supporting Information, Figure S14).

By aid of the UAT-1.4, the cell PCE has been promoted to over 20% and its I - V characteristics is shown in Figure 7a. The cell (with anti-reflection coating) has the J_{SC} of 20.76 mA cm^{-2} , V_{OC} of 1.148 V and FF of 0.843. This performance has been amongst the highest records reported so far. The impressively high FF indicates that the charge transport and charge recombination in the cell has been optimized. Compared to other works, the V_{OC} still has a large improvement space, which may be realized by further regulating the energy level structure of each layer in the cell.

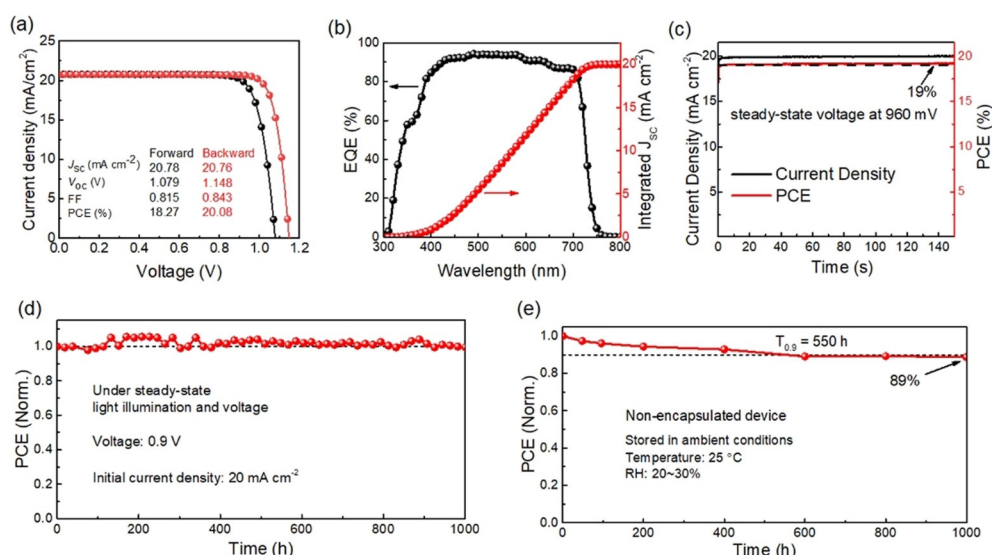


Figure 7. a) I - V characteristics of the champion cell exhibiting a PCE of 20.07%. b) External quantum efficiency (EQE) and its current density integration spectra. c) Continuous current output of the cell at a steady-state bias voltage of 0.96 V, demonstrating a PCE of over 19.2% after a 2 min operation. d) PCE tracking of the cells over 1000 h under a steady-state bias voltage of 0.9 V and a continuous white LED light illumination. The initial current density of the measured cell (initial PCE ca. 18.7%) is about 20 mA cm^{-2} . e) PCE tracking over 1000 h for the unencapsulated cell stored in ambient and dark conditions (temperature: 25°C , relative humidity: 20–30%).

External quantum efficiency (EQE) at 0 V and steady-state current output of the cell are also presented. As in Figure 7b, the integration of EQE spectrum finally leads to J_{sc} of 20.0 mA cm^{-2} , which is only 3.80% lower than the I - V result. The cell exhibits an excellent steady-state output performance; after two and a half min operation at 0.96 V, the cell gives a current density output of 20.0 mA cm^{-2} and a PCE of over 19.2%, as shown in Figure 7c. This steady-state PCE is a little higher than the average value of the forward and backward I - V results, similar to that in hybrid solar cells.

Along with high PCE, the cell also exhibits excellent photoelectric stability. For the operational stability evaluation, we have tracked the steady-state PCE output for over 1000 h at the bias voltage of 0.9 V under continuous white LED light illumination in N_2 atmosphere (N_2 flow 100 mL min^{-1}). The light intensity has been adjusted to make the cell give an initial current density of about 20 mA cm^{-2} at 0.9 V. As shown in Figure 7d, no PCE degradation can be observed after the cell works for 1000 h. But, the PCE of the control device decreased by about 20% under the same condition (Supporting Information, Figure S15). The storage stability of the cell in ambient condition was also measured. After the unencapsulated cell was stored in ambient and dark conditions (temperature: 25°C , relative humidity: 20–30 RH%) for 1000 h, 89% of its initial PCE is still retained, as in Figure 7e. Further humidity test ($40^\circ\text{C}/40\text{RH}\%$) shows that the devices in the experimental group have better stability than the devices in the control group (Supporting Information, Figure S16). It is supposed that, if being encapsulated properly, much better storage stability will be achieved. High PCE together with the excellent photoelectric stability demonstrates that the UAT additive strategy we

reported here is an effective approach to improve the performance of all-inorganic perovskite solar cells and we believe this easily operated approach can also be applicable for other perovskite-based photoelectric systems.

Conclusion

In this work, we have developed an easily operated UAT additive approach to fully exploit the coordination activity of SCN^- for high-quality CsPbI_3 films for efficient and stable all-inorganic solar cells. The UAT is derived from the hydrogen bond interaction between NH_4SCN and urea, which is realized by a simple thermal mixing process. The

coordination of SCN^- to the Pb-I octahedrons improves the CsPbI_3 film morphology and significantly suppresses defects and the non-radiative charge recombination of the film. With the optimal UAT component, we achieve a high efficiency CsPbI_3 solar cell with over 20.0% PCE and high fill factor of 0.84. Besides, the cell exhibits excellent operational stability with almost no PCE degradation after working for 1000 h. Our work here together with recent progresses demonstrates a promising development route of the CsPbI_3 related photoelectric devices, and the UAT approach is believed to be applicable for improving performance of other perovskite devices.

Acknowledgements

This work was supported by the National Natural Science Foundation of China (Nos. 51872321, 11874402, 52072402, 51627803), the Ministry of Science and Technology of the People's Republic of China (2018YFB1500101).

Conflict of interest

The authors declare no conflict of interest.

Keywords: all-inorganic perovskites · cesium lead triiodide · molten salts · solar cell · thiocyanate

[1] A. Al-Ashouri, E. Köhnen, B. Li, A. Magomedov, H. Hempel, P. Caprioglio, J. A. Márquez, A. B. M. Vilches, E. Kasparavicius,

- J. A. Smith, N. Phung, D. Menzel, M. Grischek, L. Kegelman, D. Skroblin, C. Gollwitzer, T. Malinauskas, M. Jošt, G. Matic, B. Rech, R. Schlattmann, M. Topič, L. Korte, A. Abate, B. Stannowski, D. Neher, M. Stollerfoht, T. Unold, V. Getautis, S. Albrecht, *Science* **2020**, *370*, 1300–1309.
- [2] Q. Han, Y.-T. Hsieh, L. Meng, J.-L. Wu, P. Sun, E.-P. Yao, S.-Y. Chang, S.-H. Bae, T. Kato, V. Bermudez, Y. Yang, *Science* **2018**, *361*, 904–908.
- [3] H. Li, W. Zhang, *Chem. Rev.* **2020**, *120*, 9835–9950.
- [4] National Renewable Energy Laboratory, Best research-cell efficiencies chart (2021); <http://www.nrel.gov/pv/cell-efficiency.html>.
- [5] S. H. Turren-Cruz, A. Hagfeldt, M. Saliba, *Science* **2018**, *362*, 449–453.
- [6] S. Wang, Y. Jiang, E. J. Juarez-Perez, L. K. Ono, Y. Qi, *Nat. Energy* **2016**, *2*, 16195.
- [7] Y. C. Zhao, W. K. Zhou, X. Zhou, K. H. Liu, D. P. Yu, Q. Zhao, *Light: Sci. Appl.* **2017**, *6*, e16243.
- [8] P. Gratia, G. Grancini, J. N. Audinot, X. Jeanbourquin, E. Mosconi, I. Zimmermann, D. Dowsett, Y. Lee, M. Grätzel, F. De Angelis, K. Sivula, T. Wirtz, M. K. Nazeeruddin, *J. Am. Chem. Soc.* **2016**, *138*, 15821.
- [9] A. K. Jena, A. Kulkarni, T. Miyasaka, *Chem. Rev.* **2019**, *119*, 3036.
- [10] J. Cho, J. T. DuBose, A. N. T. Le, P. V. Kamat, *ACS Mater. Lett.* **2020**, *2*, 565–570.
- [11] H. Ren, S. Yu, L. Chao, Y. Xia, Y. Sun, S. Zuo, F. Li, T. Niu, Y. Yang, H. Ju, B. Li, H. Du, X. Gao, J. Zhang, J. Wang, L. Zhang, Y. Chen, W. Huang, *Nat. Photonics* **2020**, *14*, 154–163.
- [12] T. Luo, Y. Zhang, Z. Xu, T. Niu, J. Wen, J. Lu, S. Jin, S. F. Liu, K. Zhao, *Adv. Mater.* **2019**, *31*, 1903848.
- [13] F. Zhang, H. Lu, J. Tong, J. J. Berry, M. C. Beard, K. Zhu, *Energy Environ. Sci.* **2020**, *13*, 1154–1186.
- [14] J. M. Hoffman, J. Strzalka, N. C. Flanders, I. Hadar, S. A. Cuthriell, Q. Zhang, R. D. Schaller, W. R. Dichtel, L. X. Chen, M. G. Kanatzidis, *Adv. Mater.* **2020**, *32*, 2002812.
- [15] B. E. Cohen, Y. Li, Q. Meng, L. Etgar, *Nano Lett.* **2019**, *19*, 2588–2597.
- [16] Y. Wang, M. I. Dar, L. K. Ono, T. Zhang, M. Kan, Y. Li, L. Zhang, X. Wang, Y. Yang, X. Gao, Y. Qi, M. Grätzel, Y. Zhao, *Science* **2019**, *365*, 591–595.
- [17] M. Kulbak, S. Gupta, N. Kedem, I. Levine, T. Bendikov, G. Hodes, D. Cahen, *J. Phys. Chem. Lett.* **2016**, *7*, 167–172.
- [18] W. Zhou, Y. Zhao, X. Zhou, R. Fu, Q. Li, Y. Zhao, K. Liu, D. Yu, Q. Zhao, *J. Phys. Chem. Lett.* **2017**, *8*, 4122–4128.
- [19] P. Wang, X. Zhang, Y. Zhou, Q. Jiang, Q. Ye, Z. Chu, X. Li, X. Yang, Z. Yin, J. You, *Nat. Commun.* **2018**, *9*, 2225.
- [20] Y. Yang, F. Lin, C. Zhu, T. Chen, S. Ma, Y. Luo, L. Zhu, X. Guo, *Acta Chim. Sin.* **2020**, *78*, 217.
- [21] T. Zhang, M. I. Dar, G. Li, F. Xu, N. Guo, M. Grätzel, Y. Zhao, *Sci. Adv.* **2017**, *3*, e1700841.
- [22] H. Meng, Z. Shao, L. Wang, Z. Li, R. Liu, Y. Fan, G. Cui, S. Pang, *ACS Energy Lett.* **2020**, *5*, 263–270.
- [23] Y. Wang, X. Liu, T. Zhang, X. Wang, M. Kan, J. Shi, Y. Zhao, *Angew. Chem. Int. Ed.* **2019**, *58*, 16691–16696; *Angew. Chem.* **2019**, *131*, 16844–16849.
- [24] B. Zhao, S. F. Jin, S. Huang, N. Liu, J. Y. Ma, D. J. Xue, Q. Han, J. Ding, Q. Q. Ge, Y. Feng, J. S. Hu, *J. Am. Chem. Soc.* **2018**, *140*, 11716.
- [25] K. Wang, Z. Jin, L. Liang, H. Bian, D. Bai, H. Wang, J. Zhang, Q. Wang, S. Liu, *Nat. Commun.* **2018**, *9*, 4544.
- [26] W. Ke, I. Spanopoulos, C. C. Stoumpos, M. G. Kanatzidis, *Nat. Commun.* **2018**, *9*, 4785.
- [27] S. M. Yoon, H. Min, J. B. Kim, G. Kim, K. S. Lee, S. I. Seok, *Joule* **2021**, *5*, 183–196.
- [28] Y. Wang, T. Zhang, M. Kan, Y. Zhao, *J. Am. Chem. Soc.* **2018**, *140*, 12345–12348.
- [29] A. Ho-Baillie, M. Zhang, C. F. J. Lau, F.-J. Ma, S. Huang, *Joule* **2019**, *3*, 938–955.
- [30] M. B. Faheem, B. Khan, C. Feng, M. U. Farooq, F. Raziq, Y. Xiao, Y. Li, *ACS Energy Lett.* **2020**, *5*, 290–320.
- [31] H. Uratani, K. Yamashita, *J. Phys. Chem. Lett.* **2017**, *8*, 742–746.
- [32] J. Liang, X. Han, J. H. Yang, B. Zhang, Q. Fang, J. Zhang, Q. Ai, M. M. Ogle, T. Terlier, A. A. Marti, J. Lou, *Adv. Mater.* **2019**, *31*, 1903448.
- [33] J. M. Ball, A. Petrozza, *Nat. Energy* **2016**, *1*, 16149.
- [34] Y. Li, C. Zhang, X. Zhang, D. Huang, Q. Shen, Y. Cheng, W. Huang, *Appl. Phys. Lett.* **2017**, *111*, 162106.
- [35] W. Li, J. Fan, J. Li, Y. Mai, L. Wang, *J. Am. Chem. Soc.* **2015**, *137*, 10399.
- [36] Y. Wu, A. Islam, X. Yang, C. Qin, J. Liu, K. Zhang, W. Peng, L. Han, *Energy Environ. Sci.* **2014**, *7*, 2934–2938.
- [37] W. S. Yang, J. H. Noh, N. J. Jeon, Y. C. Kim, S. Ryu, J. Seo, S. I. Seok, *Science* **2015**, *348*, 1234–1237.
- [38] D. Bi, C. Yi, J. Luo, J.-D. Décoppet, F. Zhang, S. M. Zakeeruddin, X. Li, A. Hagfeldt, M. Grätzel, *Nat. Energy* **2016**, *1*, 16142.
- [39] L. Zhu, Y. Xu, P. Zhang, J. Shi, Y. Zhao, H. Zhang, J. Wu, Y. Luo, D. Li, Q. Meng, *J. Mater. Chem. A* **2017**, *5*, 20874–20881.
- [40] W. Ke, C. Xiao, C. Wang, B. Saparov, H. S. Duan, D. Zhao, Z. Xiao, P. Schulz, S. P. Harvey, W. Liao, W. Meng, Y. Yu, A. J. Cimaroli, C. S. Jiang, K. Zhu, M. Al-Jassim, G. Fang, D. B. Mitzi, Y. Yan, *Adv. Mater.* **2016**, *28*, 5214–5221.
- [41] Q. Han, Y. Bai, J. Liu, K.-Z. Du, T. Li, D. Ji, Y. Zhou, C. Cao, D. Shin, J. Ding, A. D. Franklin, J. T. Glass, J. Hu, M. J. Therien, J. Liu, D. B. Mitzi, *Energy Environ. Sci.* **2017**, *10*, 2365–2371.
- [42] H. Kim, Y. H. Lee, T. Lyu, J. H. Yoo, T. Park, J. H. Oh, *J. Mater. Chem. A* **2018**, *6*, 18173–18182.
- [43] J. Tong, Z. Song, D. H. Kim, X. Chen, C. Chen, A. F. Palmstrom, P. F. Ndione, M. O. Reese, S. P. Dunfield, O. G. Reid, J. Liu, F. Zhang, S. P. Harvey, Z. Li, S. T. Christensen, G. Teeter, D. Zhao, M. M. Al-Jassim, M. F. A. M. van Hest, M. C. Beard, S. E. Shaheen, J. J. Berry, Y. Yan, K. Zhu, *Science* **2019**, *364*, 475–479.
- [44] H. Lu, Y. Liu, P. Ahlawat, A. Mishra, W. R. Tress, F. T. Eickemeyer, Y. Yang, F. Fu, Z. Wang, C. E. Avalos, B. I. Carlsen, A. Agarwalla, X. Zhang, X. Li, Y. Zhan, S. M. Zakeeruddin, L. Emsley, U. Rothlisberger, L. Zheng, A. Hagfeldt, M. Grätzel, *Science* **2020**, *370*, eabb8985.
- [45] C. Zheng, A. Liu, C. Bi, J. Tian, *Acta Phys.-Chim. Sin.* **2020**, *37*, 2007084.
- [46] X. Chang, J. Fang, Y. Fan, T. Luo, H. Su, Y. Zhang, J. Lu, L. Tsetseris, T. D. Anthopoulos, S. F. Liu, K. Zhao, *Adv. Mater.* **2020**, *32*, 2001243.
- [47] Y. Li, J. Shi, B. Yu, B. Duan, J. Wu, H. Li, D. Li, Y. Luo, H. Wu, Q. Meng, *Joule* **2020**, *4*, 472–489.
- [48] G. H. Wu, H. Li, J. Cui, Y. H. Zhang, S. Olthof, S. Chen, Z. K. Liu, D. P. Wang, S. Z. Liu, *Adv. Sci.* **2020**, *7*, 1903250.

Manuscript received: February 17, 2021

Revised manuscript received: March 15, 2021

Accepted manuscript online: April 1, 2021

Version of record online: May 6, 2021